Unveiling microstructural dynamics: Somatosensory-evoked response induces extensive diffusivity and kurtosis changes associated with neural activity in rodents

Andreea Hertanu[1], Tommaso Pavan[1], Ileana O. Jelescu[1]

[1]Dept. of Radiology, Lausanne University Hospital (CHUV) and University of Lausanne

KEYWORDS: Diffusion-MRI, BOLD-fMRI, microstructure, time-dependence, permeability, somatosensory response, rodent brain

ABSTRACT: Diffusion MRI (dMRI) facilitates the exploration of microstructural features within the brain owing to its sensitivity to restrictions and hindrances in the form of cell membranes or subcellular structures. As such, alterations in cell morphology and water transport mechanisms linked to neuronal activity are inherently embedded in the dMRI signal. In this context, the goal of our study was to investigate changes in Mean Diffusivity (MD) and Mean Kurtosis (MK) across the rat brain upon unilateral forepaw electrical stimulation and compare them to BOLD-fMRI mapping of brain activity. The positive BOLD response in the contralateral primary somatosensory cortex, forelimb region (S1FL) was accompanied by a significant decrease in MD in the same region, described in the literature as the result of cellular swelling and increased tortuosity in the extracellular space. For the first time, we also report a paired decrease in MK during stimulation in S1FL, most likely indicative of increased membrane permeability, as suggested by the slight decrease in exchange time estimated from kurtosis time-dependence analyses. The primary motor (M1) and the secondary somatosensory (S2) cortices, part of the cortical somatosensory processing and integration pathways, also displayed a positive BOLD response during stimulation, albeit with a lower amplitude, while MD and MK had differentiated dynamics in these two areas. In M1, the trends of MD and MK mirrored those observed in S1FL, whereas in S2, the opposite pattern was identified, that is MD and MK increased. Subcortical regions implicated in somatosensory information processing and integration, such as the thalamus and hippocampus, also exhibited an increase in MD and MK as in S2, remarkably in the absence of a discernible BOLD response. In the striatum a marginal negative BOLD response coincided with an increase in MD and MK. These findings highlight the capacity of dMRI to offer complementary functional insights into excitatory and inhibitory neural activity, potentially below the BOLD detection threshold.

1. INTRODUCTION

Neural activity involves the coordinated interplay of neurovascular and neurometabolic coupling mechanisms, where electrical signals in neurons trigger changes in blood flow and metabolism[1]. This complex process encompasses action potentials, synaptic transmission, and the integration of excitatory and inhibitory signals, contributing to essential brain functions.

By measuring the regional disparity in oxygen consumption and supply, the blood-oxygenation-level-dependent (BOLD) technique harnesses the interaction between hemodynamic and metabolic factors and provides a surrogate for brain activity[2]. Since its inception, functional Magnetic Resonance Imaging (fMRI) based on the BOLD effect (BOLD-fMRI) has become widely used and applied in the field of neuroscience. Over the years, BOLD-fMRI has been instrumental in investigating various aspects of brain function, from the intricacies of memory and attention to the examination of neurological disorders[3]. Its versatility extends beyond clinical realms, contributing to the exploration of responses to sensory stimuli, decision-making, and social cognition[4].

A less well-known coupling linking neural activity and the mechanical tissue properties was illustrated by several groups reporting transient activity-dependent neuronal and glial swelling[5–13]. The neuromorphological coupling was hypothesized as an underlying mechanism for another type of fMRI contrast based on diffusion MRI (dMRI), thought to provide a more direct mapping of neural activity as compared to BOLD[14,15]. Indeed, the spatial specificity and sensitivity of BOLD-fMRI is a challenging and stimulating debate[16] heightened by nonlinear, time-varying, and partially unknown crosstalk between hemodynamic, metabolic, and neuronal activity[17–19]. On the other hand, diffusion functional MRI (dfMRI)[14,15,20–22] leverages the sensitivity of the diffusion-weighted signal to microstructural features and provides a distinctive approach to probe cellular morphology fluctuations accompanying neural activity.

Owing to methodological hurdles, dfMRI has been subject to controversy over its ability to reflect neuromorphological changes rather than plain vascular modifications (i.e. BOLD contribution)[23–26]. However, recent studies with optimal signal-to-noise ratio (SNR)[27], ultra-high temporal resolution[28] and careful acquisition schemes minimizing vascular confounds[29] have shown that non-vascular information can be gleaned from dfMRI. Notably, time-courses of apparent diffusion coefficient (ADC) estimated from pairs of diffusion-weighted images acquired in an interleaved fashion, rather than time-courses of diffusion-weighted signals, cancel out most vascular contributions to dfMRI through T_2-weighting[20,28–30]. The typical reduction in ADC during neuronal activation reported in such dfMRI studies was attributed to

increased tortuosity in the extracellular space and cellular swelling and was detected during brain activity even in the absence of neurovascular coupling[21,31–34].

Furthermore, impairment of the water transport mechanisms taking place through aquaporin channels in astrocytes reflected as a decrease in ADC in the living rodent brain[35,36], while the addition of neural activity inhibitors in rat brain organotypic cortical cultures[37] led to a considerable decrease in the trans-membrane active water cycling mechanisms measured through relaxometry.

Aside from its role as a functional contrast, dMRI was shown to provide valuable insights into both microstructural characteristics and trans-membrane water exchange in gray matter in vivo[38–42]. In particular, the analysis of time-dependent mean diffusivity (MD) and mean kurtosis (MK) provides information on structural disorder at the micron-scale from their power-law signature[43] and/or on inter-compartment water exchange using the Kärger model[44]. Kurtosis is a measure of how water diffusion in biological tissue deviates from Gaussian diffusion[45] and is thus an excellent proxy for tissue compartmentalization, heterogeneity and complexity at the voxel-level[46], complementing the information provided by MD.

In this context, the goal of our work was to investigate changes in MD and MK values and in their diffusion time-dependence signature, associated with brain activity, and compare them to BOLD-fMRI changes. The fast kurtosis method[47,48] facilitated the estimation of MD and MK for multiple diffusion times from a reduced number of diffusion-weighted images, compatible with the brief rest and stimulus intervals typical of task fMRI block designs. The rat forepaw unilateral electrical stimulation was chosen due to its widespread adoption and extensive use as an experimental model for the exploration of brain function along the somatosensory pathways in rodents. We aimed at probing brain-wide MD and MK dynamics, including various cortical and subcortical structures reported in the literature as part of somatosensory processing and integration.

2. MATERIALS AND METHODS

2.1 Animal Preparation and Anesthesia

Experiments were approved by the local Service for Veterinary Affairs of the canton of Vaud. Ten female Wistar rats (Charles River, France) (236 $\pm$ 14g) were scanned on a 14.1T MRI system (Bruker BioSpin), using a home-built surface quadrature transceiver RF-coil. The anesthesia, stimulation and animal preparation protocols were similar to those outlined in a previous study[49]. Isoflurane anesthesia (4% for induction and 2% during setup) was used while positioning the rat into a custom-made MRI cradle. Electrical stimulation was enabled using two pairs of stainless-steel electrodes inserted in the rat forepaws, between digits 2 and 3, and

digits 4 and 5, respectively. A catheter was inserted subcutaneously on the back of the animal for medetomidine administration. Once the setup was finalized, an initial bolus of 0.1 mg/kg of medetomidine was injected, while gradually reducing the isoflurane anesthesia. Ten minutes later the isoflurane was completely interrupted, and another five minutes later a continuous medetomidine infusion at 0.1 mg/kg/h was started. The total sedation time under medetomidine was around two hours and a half, with an average respiration rate of 67 $\pm$ 18 breaths per minute and an average temperature of 38 $\pm$ 0.5°C across all rats and acquisitions. An oxygen/air supply of 20%/80% was maintained throughout the experiment. At the end of the experiment, animals were woken up by intramuscular injection of atipamezole at 0.5 mg/kg.

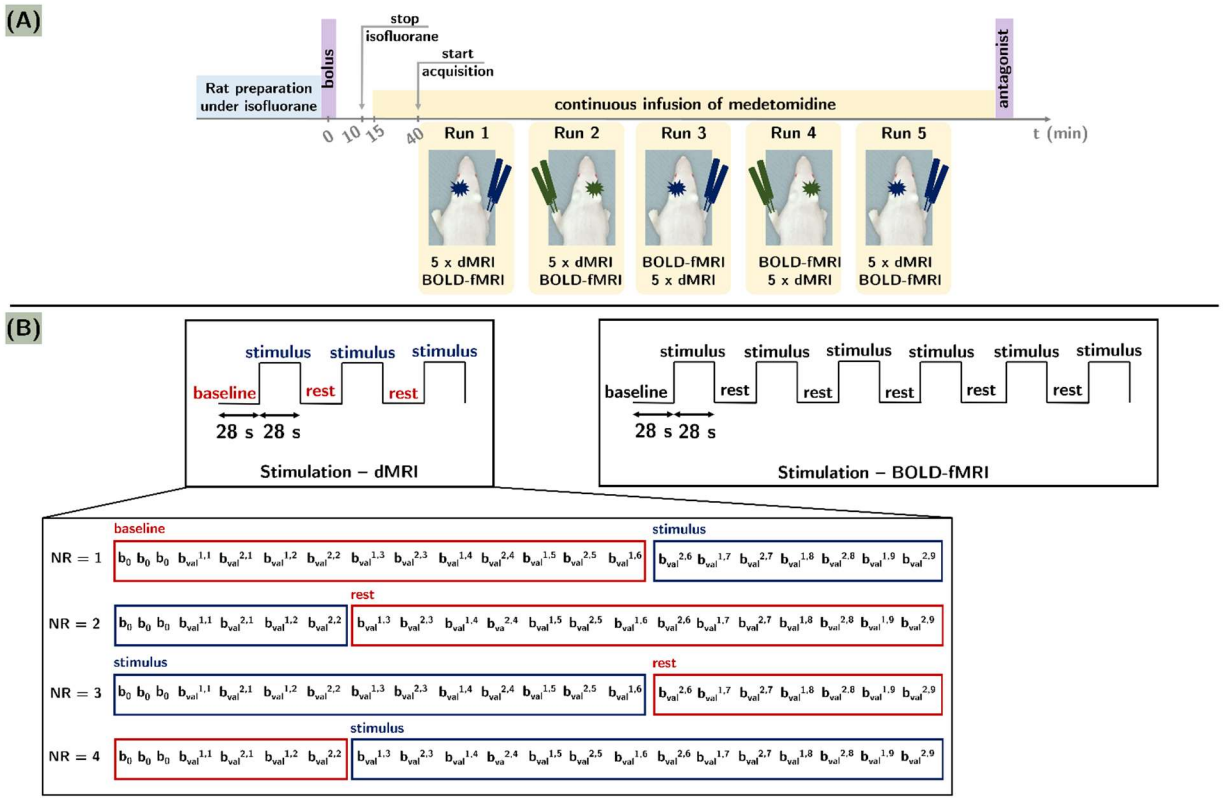

Figure 1: Data acquisition protocol – (A): Experimental timeline. (B): Each functional run included five different diffusion sequences with varying diffusion time values and one BOLD-fMRI sequence. For each diffusion time, the timing of the three epochs of alternating 28 s rest and 28 s stimulus intervals was set such as to acquire NR = 2 repetitions of 21 measurements – nine directions for two b-values ($b_{val}^{i,j}$ with i = 1; 2 ms/μm^2 and j = 9 directions) and three b_0 acquisitions for each condition (rest vs. stimulation). One BOLD-fMRI acquisition included the acquisition of 336 volumes equally spread across six epochs of alternating 28 s rest and 28 s stimulus intervals.

2.2 Paradigm Design

A custom triggering routine making use of the Transistor-Transistor Logic (TTL) pulse output delivered by the MRI scanner was implemented to generate a block paradigm for the dMRI

and BOLD-fMRI acquisitions with alternating cycles of 28 s of rest and 28 s of stimulation. The stimulation consisted of 0.3 ms pulses at 2 mA and 8 Hz frequency and was delivered by an A365 stimulus isolator interfaced with a DS8000 digital stimulator (World Precision Instruments, Stevenage, UK). Twenty-eight images for each rest and stimulus intervals were acquired during the BOLD-fMRI (TR = 1 s), and fourteen during the dMRI (TR = 2 s) block designs, respectively.

2.3 Data Acquisition

Figure 1 details the experimental design. The acquisition of functional runs comprising both dMRI and BOLD-fMRI sequences started 30 minutes after isoflurane cessation (**Figure 1A**). During that 30-minute wait time for isoflurane clearance, a B_0 map for field-map based shimming of the rat brain with default acquisition parameters and a T_2-weighted (T_2w) structural acquisition for anatomical reference were performed. The T_2w structural scan was acquired using a 2D multi-slice RARE sequence, with the following parameters: TE = 6 ms, TR = 2.5 s, matrix size 160 × 160 x 45, in-plane resolution 125 x 125 μm^2, slice thickness 0.5 mm and RARE factor = 1.

Five functional runs were acquired per rat (only four runs for two rats). Every functional run was composed of five dMRI acquisitions with different diffusion times (Δ = 9.5; 15; 20; 25; 30 ms) and one BOLD-fMRI acquisition. From one functional run to another, the forepaw used for stimulation was alternated and within each run, the order of the dMRI/BOLD-fMRI acquisitions was randomized. When tallying the total number of animals and functional runs, 24 dMRI datasets per diffusion time and per stimulated forepaw and 24 BOLD-fMRI time-series per stimulated forepaw were acquired. **Table 1** summarizes the acquisition times for the various sequences in the protocol, as well as the time needed for the acquisition of one functional run and for the entire experimental protocol for one rat.

Diffusion MRI: For each diffusion time, a monopolar Pulsed Gradient Spin Echo sequence with Echo-Planar Imaging read-out (PGSE-EPI) was used to acquire two repetitions of 21 measurements – nine directions for two b-values ($b_{val}^{i,j}$ with i = 1; 2 ms/μm^2 and j = 9 directions) and three b = 0 (b_0) acquisitions – during each condition (rest vs. stimulus). In total, 84 images were equally distributed between three epochs of alternating rest and stimulus intervals (**Figure 1B**) for a total scan time of 2 min 48 s. The remaining experimental parameters included: gradient pulse duration δ = 4 ms, TE = 48 ms, TR = 2 s, matrix size 80 x 80, 21 slices, in-plane resolution 0.25 x 0.25 μm^2, slice thickness 0.75 µm and partial Fourier acceleration factor of 1.1 in the phase direction. In a separate scan, three b_0 images were acquired with reversed EPI phase-encode direction, without stimulation, for spatial distortion correction.

BOLD-fMRI: Data was acquired using a gradient-echo EPI (GE-EPI) sequence with the following parameters: TE = 11.1 ms, TR = 1 s, and matrix size, number of slices, in-plane resolution and slice thickness matching to the dMRI acquisitions (80 x 80, 21, 250 x 250 μm^2 and 750 µm, respectively). A partial Fourier acceleration factor of 1.2 was employed for the phase direction. A total number of 336 images were acquired during six epochs of alternating rest and stimulus intervals (**Figure 1B**), resulting in 168 images for each rest and stimulus condition, collected in 5 min 36 s. In a separate scan, ten GE-EPI images were acquired with reversed EPI phase-encode direction, without stimulation, for spatial distortion correction.

Phase encoding:	**Forward**	**Reverse**
dMRI acquisition	2 min 48 s	8 s
BOLD-fMRI acquisition	5 min 36 s	10 s
1 run (5xdMRI + fMRI)	19 min 54 s	
B_0 map	1 min 20 s	
T_2w	6 min 40 s	
1 rat dataset	1 h 47 min 30 s	

Table 1: Acquisition times for the individual dMRI and BOLD-fMRI sequences, one functional run, the B0 map, the T2w structural sequence and finally, for the entire protocol for one rat. For each functional run, one dMRI and one BOLD-fMRI reverse-phase encode acquisition was performed for spatial distortion correction. The total duration of one functional run corresponds to the acquisition times of five dMRI sequences with different diffusion times, one BOLD-fMRI sequence, and the two reverse-phase encode acquisitions. The duration of the entire protocol for one rat includes the acquisition of the B0 map, the structural T2w image and five functional runs.

2.4 Data Processing

Diffusion MRI: Pre-processing steps, conducted in python (v.3.9, Python Software Foundation), are illustrated in **Figure 2.** The first step (**Figure 2A**) included denoising[50,51], Gibbs unringing[51,52], topup[53] and eddy[54] correction for each run separately. A rat brain mask was estimated using the atlasbrex[55] routine. The two repetitions of diffusion-weighted volumes and the b_0 images acquired for each rest and stimulus condition were averaged, and the resulting 19 images per condition were used to perform a voxel-wise estimation[47,48] of MD^{rest}, $MD^{stimulus}$, MK^{rest} and $MK^{stimulus}$ maps for each diffusion time using Matlab (v.R2021b, MathWorks Inc.) scripts (https://github.com/sunenj/Fast-diffusion-kurtosis-imaging-DKI). Voxels yielding unphysical values due to noise or partial volume (e.g. negative kurtosis or diffusivity) were excluded from further analysis.

BOLD-fMRI: Every BOLD-fMRI time-series went through Gibbs unringing[51,52] and topup correction[53] (**Figure 2A**). Prior to the generalized linear model (GLM) analysis in SPM12

(http://www.fil.ion.ucl.ac.uk/spm/software/spm12/), time-series were slice-timing corrected and minimally smoothed (gaussian smoothing kernel with 0.1 x 0.1 x 1 mm^3 size). High-pass filtering with a cut-off frequency of 0.01 Hz applied on the time-courses ensured the removal of low-frequency noise and drifts. A rat brain mask was estimated using the atlasbrex[55] routine for the BOLD-fMRI volumes. For the GLM analysis, a boxcar[49] response function was used, and statistically significant voxels were detected using a p-value threshold of 0.05 with family-wise error correction. To ensure maximum detection sensitivity, no threshold was applied on the size of the clustered voxels. Prior to ROI-wise quantifications, a brain mask excluding voxels with a signal lower than 10% of the signal measured in the cortex was generated. This step aimed to remove voxels from deeper brain regions where coil sensitivity was heavily attenuated.

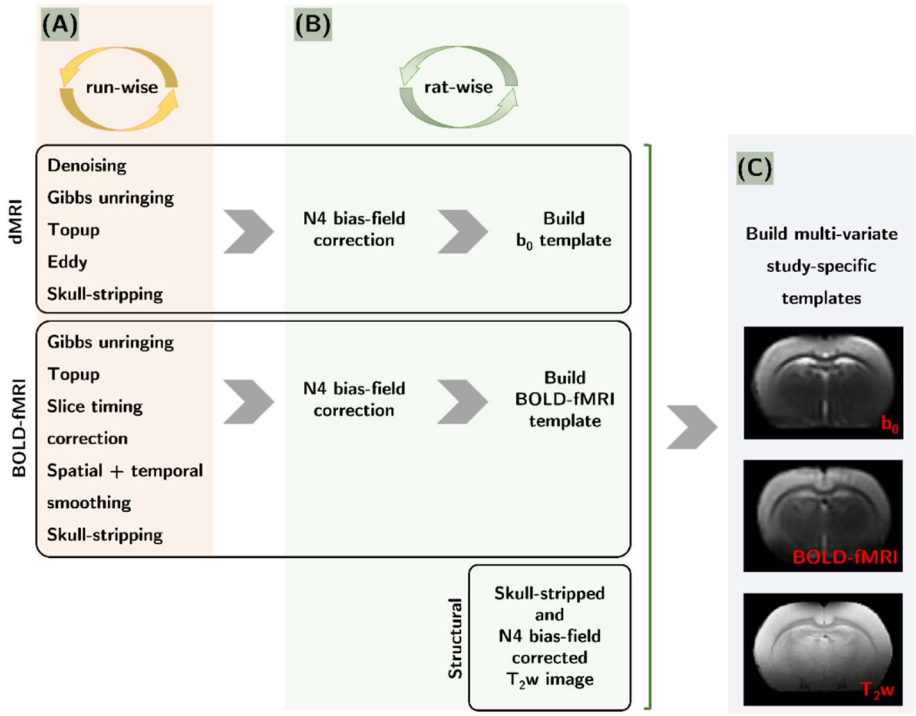

Figure 2: Pre-processing steps – (A): The five diffusion datasets from each functional run were pooled and underwent denoising, Gibbs-unringing, topup and eddy correction, and skull-stripping, while for the BOLD-fMRI time-series topup, slice-timing correction, spatial and temporal smoothing, and skull-stripping were applied for each functional run. (B): Images were then N4 bias-field corrected and the extracted b_0 images and BOLD-fMRI time-series were used to build corresponding templates for each rat. The skull-stripped and N4 bias-field corrected T_2w images were jointly used along with the b_0 and BOLD-fMRI rat-specific templates to construct multi-variate study-specific templates intended to facilitate the propagation of brain segmentations from the WHS T_2w atlas into the dMRI and BOLD-fMRI individual rat spaces.

2.5 Quantification

ANTs[56] was employed to generate rat-specific b_0 and BOLD-fMRI templates from individual images after applying N4 bias-field correction[57] (**Figure 2B**). Individual T_2w images were also

N4 bias-field corrected and skull-stripped and then used jointly along with the b_0 and BOLD-fMRI rat-specific templates to generate study-specific multivariate b_0/BOLD-fMRI/T_2w templates (**Figure 2C**). The WHS atlas[58] was registered onto our study-specific T_2w template and the transformation was applied to the WHS atlas segmentation. The multi-variate templates facilitated the propagation of the brain segmentations into the native dMRI and BOLD-fMRI spaces of each rat.

The segmented regions-of-interest (ROIs) are illustrated in **Figure S1** (Supporting Information) and included: primary somatosensory cortex, forelimb area (S1FL), secondary somatosensory cortex (S2), primary motor cortex (M1) as cortical ROIs expected to be involved in the somatosensory processing, thalamus (Tha), striatum (CPu) and hippocampal subfields (Hip) as subcortical ROIs expected to be part of subcortical somatosensory relays, and secondary motor cortex (M2), cingulate cortex (ACC), retrosplenial cortex (RSC) and posterior parietal cortex (PPC) as control cortical ROIs.

Quantifications in each ROI were done in the left hemisphere and were reported as contralateral when the right forepaw was stimulated (expected response in the left S1FL), and ipsilateral when the left forepaw was stimulated (little to no response expected in left S1FL, as the main response should be in the right S1FL).

Diffusion MRI: The mean and standard deviation for MD and MK in each ROI were calculated for all diffusion times, runs and rats in the rest and stimulus conditions and were then grouped by stimulated forepaw. The average MD and MK values ($\pm$ standard error) for each forepaw and each condition were computed to yield $MD^{rest}(\Delta)$, $MD^{stimulus}(\Delta)$, $MK^{rest}(\Delta)$ and $MK^{stimulus}(\Delta)$ curves in all the investigated brain regions contralaterally and ipsilaterally. $MD(\Delta)$ and $MK(\Delta)$ time-dependence analyses were conducted in S1FL only. Power-laws for structural disorder[43] and the analytical formulation of time-dependent kurtosis from the two-compartment Kärger model with exchange[44] were fit to the experimental curves to evaluate potential differences in morphology and permeability between the rest and stimulus conditions. The following equations were used for 1D structural disorder (equations 1 and 3), 2D-3D structural disorder (equations 2 and 4) and the Kärger exchange model (equation 5):

$$MD(\Delta) \cong D_\infty + 2A * \Delta^{-1/2} \quad (1)$$

$$MD(\Delta) \cong D_\infty + A\frac{\ln(\Delta/t_c)}{\Delta} \quad (2)$$

$$MK(\Delta) \cong K_\infty + 2A * \Delta^{-1/2} \quad (3)$$

$$MK(\Delta) \cong K_\infty + A\frac{\ln(\Delta/t_c)}{\Delta} \quad (4)$$

$$MK(\Delta) \cong K_0\frac{2t_{ex}}{\Delta}\left[1 - \frac{t_{ex}}{\Delta}\left(1 - e^{-\Delta/t_{ex}}\right)\right] \quad (5)$$

BOLD-fMRI: Beyond the GLM analysis, the average and standard deviation of the BOLD-fMRI signal was calculated in each ROI and each volume of the time-series. For each time-series, the BOLD signal in each epoch was normalized by the average signal in the 14 s preceding the stimulation. Then, the BOLD signal response function was calculated by averaging across all epochs, runs and rats. In a separate analysis, and to make a fairer comparison to the MD and MK measures which result from diffusion-weighted images acquired across multiple blocks of rest and stimulation (i.e. yielding one MD and MK estimate per condition), the BOLD signal was also averaged across all timepoints of the rest and stimulus intervals, respectively. As a result, one BOLD amplitude estimate ($\pm$ standard error) per condition was obtained.

2.6 Statistical analyses

All analyses were carried out in RStudio (v.2023.12.1, R Foundation for Statistical Computing), using the lme4 package[59]. Correction for multiple comparisons using the false discovery rate (FDR) method was applied on each metric (BOLD, MD and MK) separately.

Diffusion MRI: The mean MD and MK values quantified in each ROI and for each diffusion time, run, rat and the two conditions were used for the statistical analyses (240 total measurements per ROI). The hierarchical structure of our dMRI data indicated that a mixed effects model would be the most suitable approach. The choice criteria for the statistical model are detailed in **Table S1** (Supporting Information). Our factorial design included two main effects: the condition of the rat during the measurement (i.e, rest vs. stimulus) and the diffusion time (five different values) in order to detect statistically significant changes between the rest and stimulus measurements on the one hand, and between measurements at various diffusion times (time-dependence) on the other hand. Two random effects were also considered - the run and the subject indexes. The run index may contribute to random variability in the data due to its temporal spacing in relation to the switch-off of isoflurane anesthesia, slight variations in the temperature and respiration rate across the runs and biological variability in the rat response to the forepaw stimulus. The subject index represents the random variability introduced by biological differences between the rats.

BOLD-fMRI: The average BOLD amplitudes estimated for the rest and stimulus conditions were used to determine statistically significant differences in each ROI (48 total measurements per ROI). The statistical design including the state of the rat during the measurement (i.e, rest vs. stimulus) was the most suitable for the evaluation of significant differences as indicated in **Table S2** (Supporting Information).

3. RESULTS

3.1 BOLD-fMRI time-series analyses

A few examples of spatial localization for the statistically significant clusters ($p < 0.05$) resulting from the GLM analysis conducted on the BOLD-fMRI time-series data corresponding to unilateral right forepaw stimulation are illustrated in **Figure S2** (Supporting Information). Globally, the activated area extended over a minimum of five adjacent slices and was mainly localized in the left primary somatosensory cortex. The total number of voxels in the activated region for the 24 datasets (from ten rats) ranged from 14 to 431, with a mean of 179 voxels/cluster. On average, around 80% of the voxels were situated within the primary somatosensory cortex, while the remaining 20% were distributed between the motor cortex (17%) and the secondary somatosensory cortex (3%). Only for five datasets out of twenty-four the activated area presented sparse voxel distributions in the thalamus (< 5%), and less than five datasets presented sparse voxel distributions in the cingulate cortex (<3%), retrosplenial cortex (<3%) auditory cortex (<1%), hippocampal subfields (<0.5%) and subicular complex (<0.7%). Percentages are defined with respect to the number of significant voxels detected in the whole brain. The GLM analysis did not unveil any activation clusters in the ipsilateral hemisphere.

3.2 Rest vs. stimulus BOLD, MD and MK changes

An example of BOLD image, MD and MK parametric maps for one rat is displayed in **Figure 3** to illustrate the overall quality of our data.

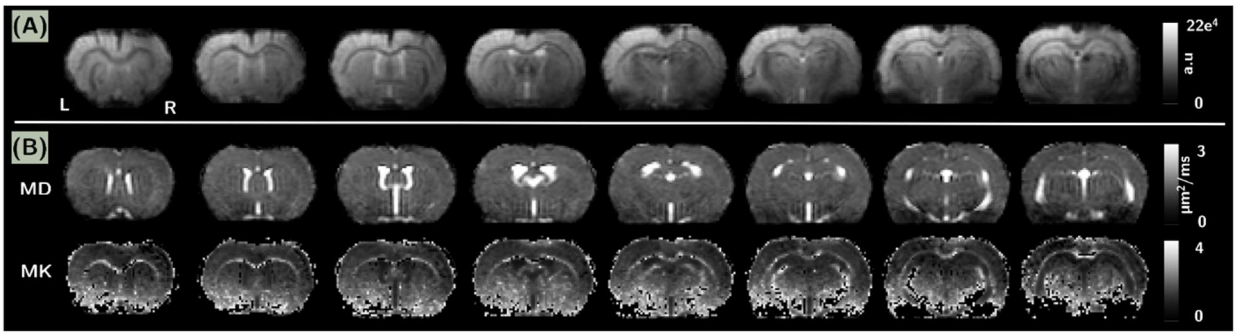

Figure 3: Illustration of the quality of (A): the BOLD-fMRI images after the pre-processing steps and (B): the parametric MD and MK maps, in rostro-caudal slices for one rat. The displayed MD and MK maps correspond to a diffusion time of Δ=9.5 ms.

Statistically significant amplitude changes in the average BOLD signal and MD and MK metrics during the stimulus condition are reported as a percentage of increase or decrease with respect to the rest condition in **Table 2.** The associated p-values are reported in **Table S3**

(Supporting Information). We underline that the significant BOLD changes result from the analysis of the normalized time-series signal averaged across each ROI for all rest vs. stimulus timepoints. This approach mirrors the sensitivity of MD and MK estimates, which are also averaged across entire anatomical ROIs and result from diffusion-weighted measurements spread across all the rest vs. stimulus timepoints during each functional acquisition. For MD and MK, the amplitude change was calculated for each diffusion time and only the maximum value was reported. The diffusion times corresponding to the maximum amplitude change are reported in **Table S4** (Supporting Information).

% change		S1FL	M1	S2	Tha	Hip	CPu
Contralateral	BOLD	+1.2 (***)	+0.2 (*)	+0.3 (**)	-	-	-0.1
	MD	-1.1 (***)	-1.2 (***)	+1.5 (***)	+1.9 (***)	+1.6 (***)	+1.4 (***)
	MK	-4.9 (***)	-	-	+2.4 (***)	+2.4 (***)	+1.5 (*)
Ipsilateral	BOLD	-	-	-	-	-	-
	MD	-0.8 (*)	-	+1.6 (***)	+1.6 (***)	+1.3 (***)	+1.6 (***)
	MK	-	-	+3.1 (*)	+1.9 (**)	-	+1.7 (***)

Table 2: The percentage of signal change during stimulation with respect to the resting condition in the ROIs presenting significant modifications. The BOLD signal changes represent the average relative difference between all rest and stimulus time-points, while the MD and MK changes represent the maximum relative difference between the rest and stimulus conditions obtained across the five diffusion times. The polarity of the signal change is highlighted in colors (green and red for positive and negative changes, respectively). * $p < 0.05$, ** $p < 0.01$, *** $p < 0.001$, with FDR correction for multiple comparisons. The CPu presented a weakly significant BOLD signal decrease ($p < 0.05$) contralaterally that did not survive correction for multiple comparisons. Globally, the absolute amplitude of the significant MD and MK changes is higher than for BOLD.

Primary sensorimotor cortices

The main brain region involved in processing forelimb stimulation – S1FL – presented an average BOLD signal increase of +1.2% contralaterally (**Table 2**, **Figure 4A**). This finding is consistent with the location of the significant signal variations detected at the voxel level in the GLM analysis (**Figure S2,** Supporting Information) and the positive response function calculated in the ROI by averaging across all epochs and all rats (**Figure S3A**, Supporting Information). Ipsilaterally, BOLD signal changes in whole ROI were not significant, consistent with the response function displayed in **Figure S3A** (Supporting Information). On the other

hand, diffusion metrics presented a significant decrease in contralateral S1FL during the stimulus condition (**Figures 4B,D**), with maximum amplitudes of -1.1% and -4.9% for MD and MK, respectively (**Table 2**). Ipsilaterally, a weak significant decrease in MD during the stimulation was also found, while no significant changes in MK were detected (**Figures 4C,E**).

In contralateral M1, the average BOLD signal increase (**Figure 4F**) was significant, but lower in amplitude than in S1FL, reaching only +0.2% (**Table 2**). The response function in **Figure S3B** (Supporting Information) shows a clear increase in the BOLD signal during the stimulation time-window. Furthermore, a significant MD decrease with an amplitude of -1.2%, remarkably similar in effect size to the MD decrease in S1FL, was measured (**Figure 4G, Table2**). No significant changes were found ipsilaterally (**Figures 4H**,**J**).

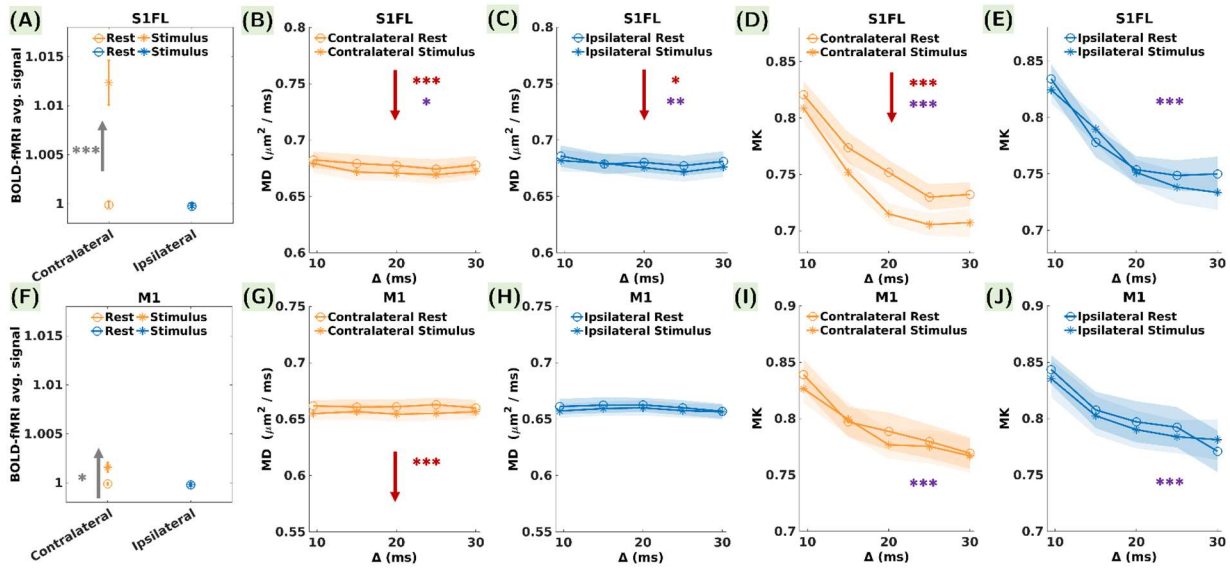

Figure 4: Average BOLD signal, MD and MK during the rest and stimulus conditions in the primary sensorimotor cortices: (A-E) S1FL and (F-J) M1, contralaterally (blue) and ipsilaterally (orange). For BOLD, statistical differences between the mean across the rest and stimulus time-points are indicated in gray asterisks (the error bars represent the standard error calculated over twenty-four measurements in each condition). Red and purple asterisks in the MD and MK plots indicate statistically significant differences between the rest and stimulus conditions and between the diffusion time values, respectively (the error bars represent the standard error calculated over twenty-four measurements in each condition and each diffusion time). P-values are reported as: * $p < 0.05$, ** $p < 0.01$, *** $p < 0.001$ (FDR correction for multiple comparisons). Upwards/downwards red and gray arrows indicate an increase/decrease in the quantified metrics. The significant average BOLD increase in contralateral S1FL was accompanied by a significant decrease in MD and MK, while in contralateral M1 a significant average BOLD increase was paired with a significant decrease in MD only. Ipsilaterally, only MD in S1FL decreased significantly.

Secondary sensorimotor cortices

Contralateral S2 also presented an increase in the average BOLD signal during stimulation, with an amplitude of +0.3% (**Figure 5A**, **Table 2**) and a distinctive positive response function (**Figure S3C**, Supporting Information). Ipsilaterally, there were no significant BOLD signal variations (**Table 2**). However, a significant increase was found in contralateral S2 for MD (**Figure 5B**), contrasting the trends in S1FL and M1. Remarkably, the MD increase was significant both contra- and ipsilaterally (**Figure 5C**), with maximum amplitudes of +1.5% and +1.6%, respectively (**Table 2**). A significant MK increase of +3.1% was measured only ipsilaterally (**Figure 5E**). In contralateral and ipsilateral M2, no significant changes were found for BOLD, MD or MK (**Figures 5F-J**).

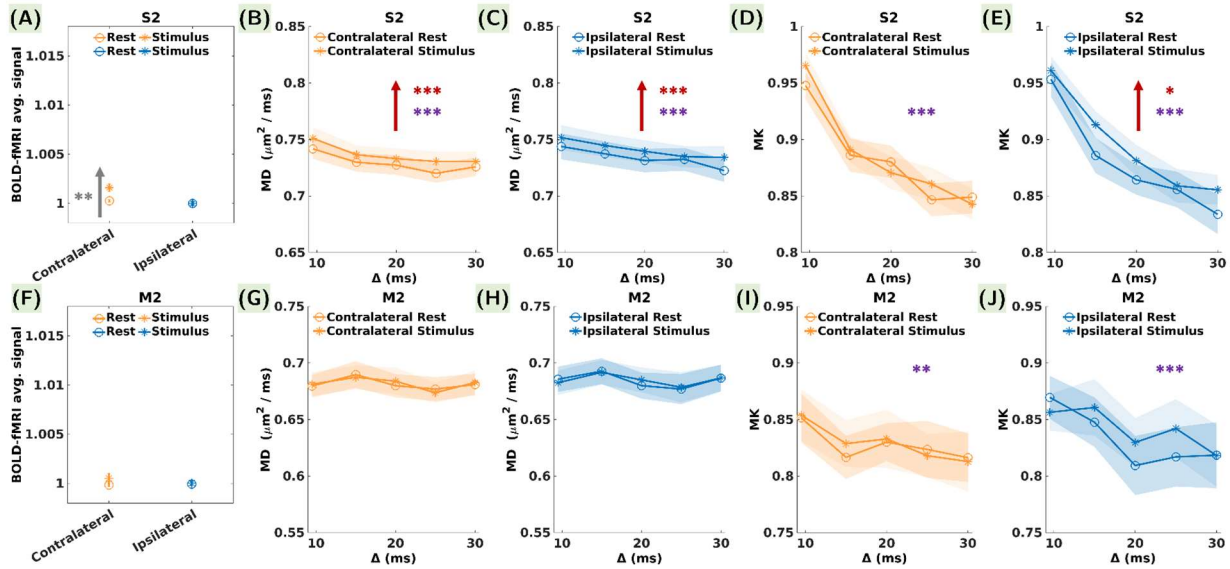

Figure 5: Average BOLD signal, MD and MK during the rest and stimulus conditions in the secondary sensorimotor cortices: (A-E) S2 and (F-J) M2, contralaterally (blue) and ipsilaterally (orange). For BOLD, statistical differences between the mean across the rest and stimulus time-points are indicated in gray asterisks (the error bars represent the standard error calculated over twenty-four measurements in each condition). Red and purple asterisks in the MD and MK plots indicate statistically significant differences between the rest and stimulus conditions and between the diffusion time values, respectively (the error bars represent the standard error calculated over twenty-four measurements in each condition and each diffusion time). P-values are reported as: * $p < 0.05$, ** $p < 0.01$, *** $p < 0.001$ (FDR correction for multiple comparisons). Upwards/downwards red and gray arrows indicate an increase/decrease in the quantified metrics. In contralateral S2 a significant BOLD signal increase was accompanied by a significant increase in MD and MK, contrasting the results in the primary sensorimotor cortices. Ipsilaterally, a significant increase was found only for MK. In M2, no significant changes were found in BOLD signal, MD or MK both contralaterally and ipsilaterally.

Subcortical brain regions

In the Tha and the Hip, no significant changes in the average BOLD signal were found contralaterally and ipsilaterally (**Figures 6A,F**) and the response functions did not display any changes during stimulation (**Figures S4E,F**). Remarkably, contralateral CPu displayed a weak decrease in the average BOLD signal (**Figure 7K, Table S1**) with an amplitude of -0.1% and a negative response function (**Figure S3G**, Supporting Information). However, the p-value was no longer significant after correction for multiple comparisons.

Similarly to S2, the subcortical brain regions presented a significant increase in MD both contralaterally and ipsilaterally (**Figures 6B,C,G,H,L and M**), with amplitudes in the range of +1.3 to +1.9%. MK also increased significantly both contralaterally and ipsilaterally in all subcortical ROIs (except for ipsilateral Hip) with amplitudes ranging from +1.5% to +2.4% (**Figures 6D,E,I,J,N and O**).

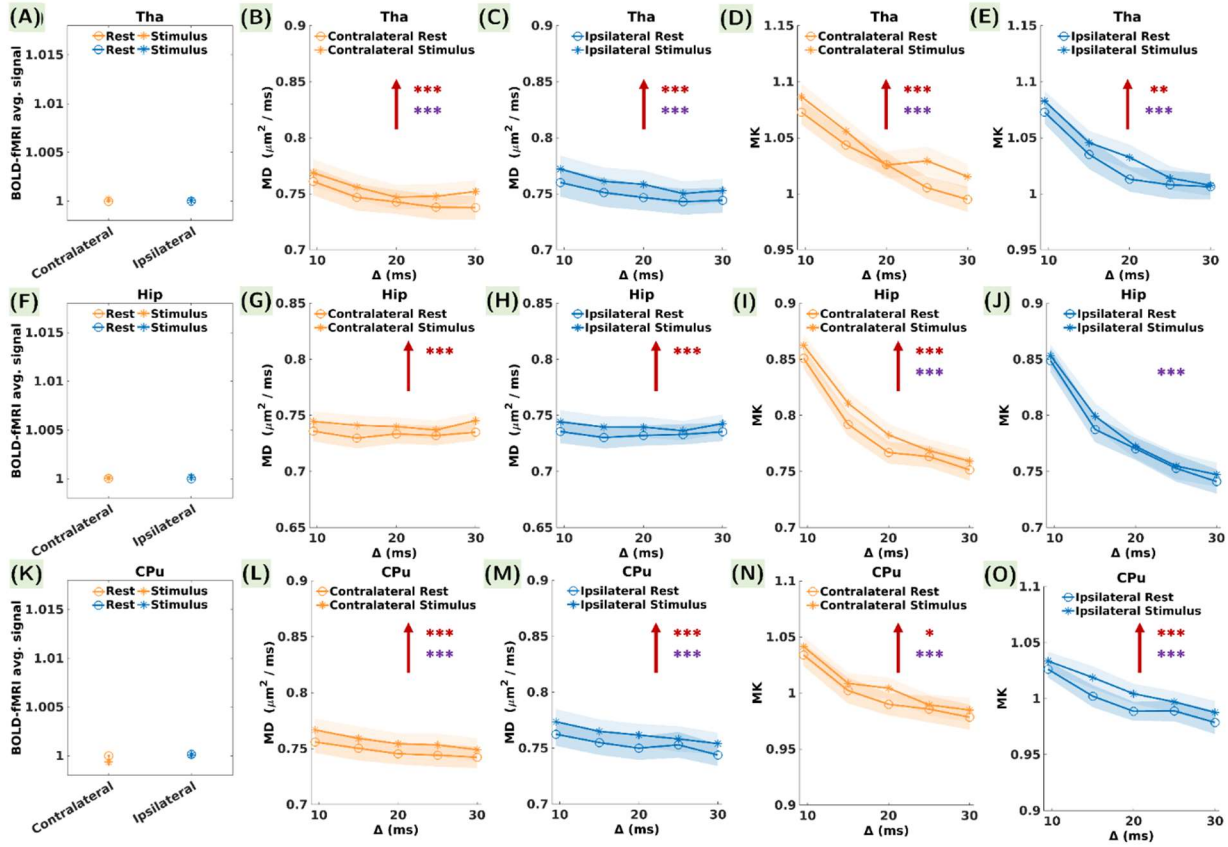

Figure 6: Average BOLD signal, MD and MK during the rest and stimulus conditions in the subcortical somatosensory relays (A-E) Tha, (F-J) Hip and (K-O) CPu, contralaterally (blue) and ipsilaterally (orange). For BOLD, statistical differences between the mean across the rest and stimulus time-points are indicated in gray asterisks (the error bars represent the standard error calculated over twenty-four measurements in each condition). Red and purple asterisks in the MD and MK plots indicate statistically significant differences between the rest

and stimulus conditions and between the diffusion time values, respectively (the error bars represent the standard error calculated over twenty-four measurements in each condition and each diffusion time). P-values are reported as: * $p < 0.05$, ** $p < 0.01$, *** $p < 0.001$ (FDR correction for multiple comparisons). Upwards/downwards red and gray arrows indicate an increase/decrease in the quantified metrics. Overall, all subcortical ROIs displayed a significant increase in MD and MK during stimulation bilaterally, and only contralateral CPu displayed a very weak decrease in BOLD, however non-significant after FDR correction for multiple comparisons.

Control cortical brain regions

ACC, RSC and PPC did not display any significant changes in the average BOLD signal, MD or MK between the rest and stimulus conditions (**Figure 7**).

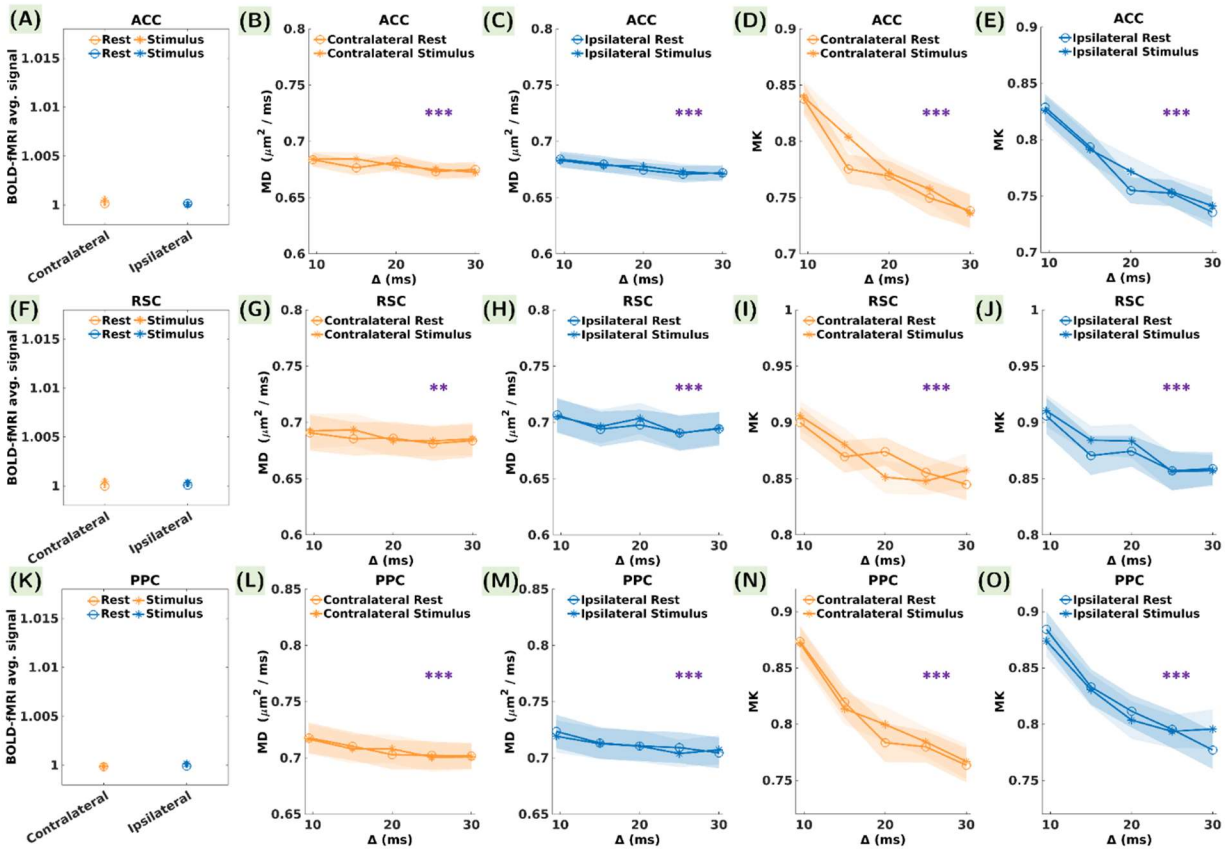

Figure 7: Average BOLD signal, MD and MK during the rest and stimulus conditions in control cortical brain regions (A-E) ACC, (F-J) RSC and (K-O) PPC, contralaterally (blue) and ipsilaterally (orange). The error bars represent the standard error calculated over twenty-four measurements in each condition for BOLD and over twenty-four measurements in each condition and each diffusion time for MD and MK. No statistically significant differences were noticed between the rest and stimulus conditions for BOLD, MD or MK. Purple asterisks in the MD and MK plots indicate statistically significant differences between the diffusion time values. P-values are reported as: * $p < 0.05$, ** $p < 0.01$, *** $p < 0.001$ (FDR correction for multiple comparisons).

To summarize, in the primary sensorimotor cortex, we report a significant decrease in MD in bilateral S1FL and contralateral M1, and a significant decrease in MK in contralateral S1FL. These changes were paralleled by a significant BOLD signal increase in contralateral S1FL and

M1. In the secondary somatosensory cortex and subcortical regions, we report an increase in MD in bilateral S2, Tha, Hip and CPu, and an increase in MK in bilateral Tha and CPu, ipsilateral S2 and contralateral Hip, while at the BOLD signal level we only found a very mild decrease in contralateral CPu. Globally, significant MD and MK changes were consistently on the order of 1% or higher throughout the investigated brain regions, while the reported significant BOLD signal changes were higher than 1% in S1FL and lower than 0.5% in S2 and M1.

3.3 MD and MK time-dependence

Measurable time-dependence was found for MD and MK bilaterally in most brain regions, except for MD in bilateral M1, M2 and Hip. The corresponding p-values are reported in **Table S5** (Supporting Information).

S1FL time-dependence analysis

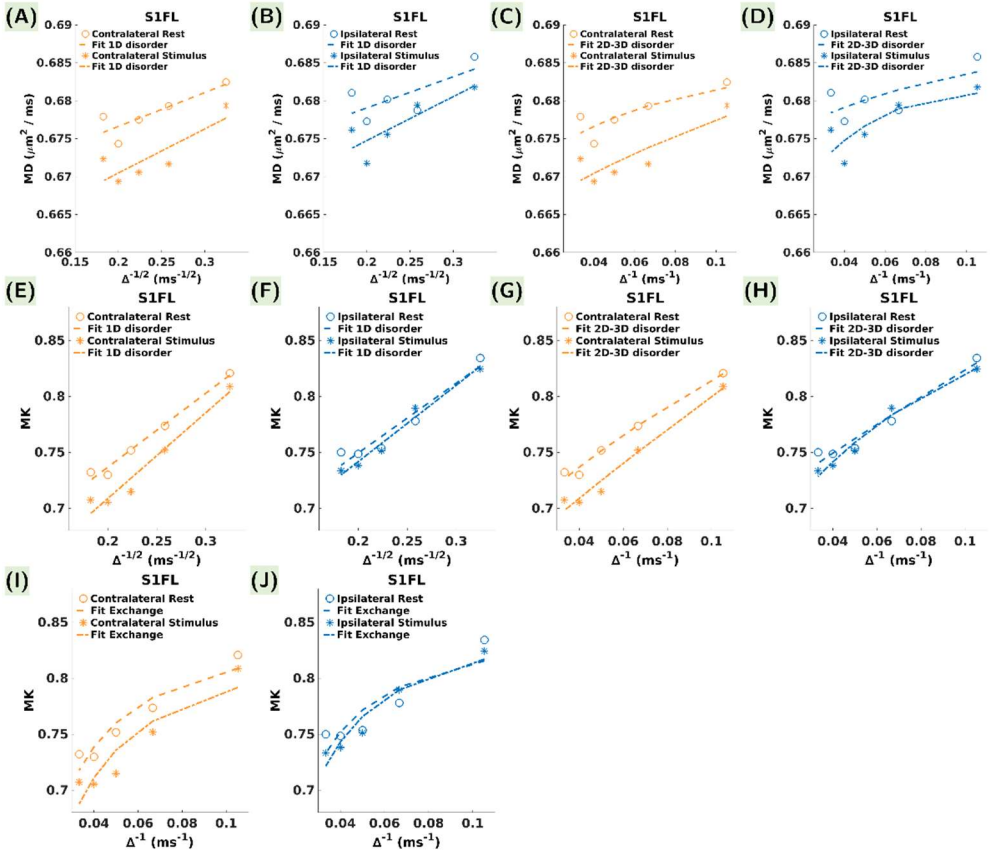

Figure 8: Power-law fit curves (dotted lines) in S1FL for (A,B) structural 1D disorder to MD time-dependence, (C,D) structural 2D-3D disorder to MD time-dependence, (E,F) structural 1D disorder to MK time-dependence, (G,H) structural 2D-3D disorder to MK time-dependence), and (I,J) the Kärger model kurtosis to MK time-dependence.

The lower corrected Akaike information criterion (AICc) obtained by fitting a 1D structural disorder model (equation 1) to the MD(Δ) decay in contralateral and ipsilateral S1FL (**Figures 8A,B**) indicates that 1D disorder from water inside cell processes had a superior contribution to the MD time-dependence as compared to 2D-3D disorder (equation 2, **Figures 8C,D**) from water in the extra-cellular space (**Table 3**). However, when comparing rest vs. stimulus MD time-dependent features, a similar AICc, as well as similar fit coefficients strongly suggested that the signature of 1D structural disorder was similar in both conditions. Similar trends were observed when fitting the structural disorder models to MK(Δ) (equations 3 and 4), but with higher AICc values than for MD(Δ) (**Figures 8E-H**, **Table 4**), suggesting structural disorder models alone explain MK time-dependence insufficiently as compared to MD time-dependence.

MD	**1D disorder**		**2D-3D disorder**		
	A	**D_∞**	**A**	**t_c (ms)**	**D_∞**
Contralateral Rest	**0.02 ± 0.008**	**0.67 ± 0.004**	**0.08 ± 0.26**	**2.03 ± 6.4**	**0.67 ± 0.02**
	AICc = -42		**AIC = -21**		
Contralateral Stimulus	**0.03 ± 0.01**	**0.66 ± 0.005**	**0.04 ± 0.33**	**0.29 ± 7.1**	**0.66 ± 0.02**
	AICc = -38		**AIC = -19**		
Ipsilateral Rest	**0.02 ± 0.01**	**0.67 ± 0.006**	**0.05 ± 0.37**	**1.37 ± 13.1**	**0.67 ± 0.02**
	AICc = -38		**AIC = -18**		
Ipsilateral Stimulus	**0.03 ± 0.01**	**0.66 ± 0.005**	**0.22 ± 0.36**	**3.37 ± 2.8**	**0.66 ± 0.02**
	AICc = -39		**AIC = -18**		

Table 3: Results of the 1D and 2D-3D structural disorders fit on the MD time-dependence. The lower AICc for 1D structural disorder and the lower uncertainty of the A and D_∞ estimated coefficients, point towards a dominant contribution of 1D structural disorder to the MD time-dependence. Differences in AICc, A and D_∞ are minimal between the rest and stimulus conditions, suggesting that 1D structural disorder is not the driving mechanism behind the significant differences in MD. For 2D-3D structural disorder, both the AICc and the uncertainty of the estimated coefficients are high, thus limiting the interpretation of the results.

When fitting the Kärger model kurtosis (equation 5) to MK(Δ) (**Figures 8I,J**), the estimated exchange time was found to be shorter during stimulation ($t_{ex}^{stimulus} = 45.1 \pm 12.0$ ms vs. $t_{ex}^{rest} = 53.8 \pm 11.1$ ms contralaterally, and $t_{ex}^{stimulus} = 51.5 \pm 8.8$ ms vs. $t_{ex}^{rest} = 60.7 \pm 19.5$ ms ipsilaterally), suggesting increased membrane permeability during the stimulus condition. However, the difference in exchange time during rest and stimulation was in the range of the estimation uncertainty (**Table 4**). Comparable AICc between the 1D structural

disorder and the exchange models indicate that both mechanisms drive the MK time-dependence, thus possibly biasing the t_{ex} estimate.

MK	1D disorder		2D-3D disorder			Kärger model	
	A	K_∞	A	t_c (ms)	K_∞	K_0	t_{ex} (ms)
Contralateral Rest	0.33 ± 0.03	0.60 ± 0.01	0.43 ± 0.72	0.27 ± 1.36	0.66 ± 0.05	0.86 ± 0.02	53.8 ± 11.1
	AICc = -30		AICc = -11			AICc = -21	
Contralateral Stimulus	0.38 ± 0.05	0.56 ± 0.02	0.17 ± 1.11	8.8e-4 ± 0.05	0.64 ± 0.07	0.85 ± 0.03	45.1 ± 12.0
	AICc = -24		AICc = -7			AICc = -17	
Ipsilateral Rest	0.31 ± 0.05	0.62 ± 0.02	0.14 ±1.2	6.3e-4 ± 0.05	0.69 ± 0.07	0.86 ± 0.03	60.7 ± 19.5
	AICc = -24		AICc = -6			AICc = -18	
Ipsilateral Stimulus	0.34 ± 0.03	0.61 ± 0.02	1.03 ± 0.91	1.52 ± 1.73	0.63 ± 0.06	0.87 ± 0.02	51.5 ± 8.8
	AICc = -28		AICc = -9			AICc = -23	

Table 4: Results of the 1D and 2D-3D structural disorders, and Kärger model kurtosis fit on the MK time-dependence. Equivalent to results for the MD time-dependence, the 1D structural disorder fit presented lower AICc and uncertainty on the estimated parameters as compared to the 2D-3D structural disorder fit. Structural disorder and exchange mechanisms are both contributing to the MK time-dependence, likely affecting the estimation of the exchange time using the Kärger exchange model. A decrease in exchange time during stimulation was nonetheless found bilaterally.

4. DISCUSSION

In this paper, we report brain region-specific changes in MD and MK related to a task of forepaw electrical stimulation. In particular, we present the first evidence of a decrease in MK, paired with previously reported decreased MD[20,30], associated with neuronal activity within the primary somatosensory cortex in the rodent brain, and an increase in MD and MK in the secondary somatosensory and subcortical areas. These modifications did not parallel changes in the BOLD signal in a systematic way, pointing to a disconnection of underlying functional contrast sources between diffusion weighting and BOLD.

4.1 Somatosensory cortical and subcortical pathways

While the primary somatosensory cortex is generally the main focus in functional studies of forepaw or hindpaw electrostimulation[60–68], a detectable BOLD response was previously reported[69–76] in the sensorimotor and subcortical areas found to present task-induced MD and

MK changes in the current study. In addition to activation in the contralateral S1FL, a weak BOLD response was also formerly detected ipsilaterally[74,75] and was attributed to somatosensory activity via inter-hemispheric sensory pathways[75]. Furthermore, a positive BOLD response in the contralateral M1 was found in several other studies[70,71,73–76], although it was construed as an overflow in some cases[70] or an antidromic stimulation of efferent motor fibers in others[71,73]. Nevertheless, studies using retrograde tracing techniques have clearly demonstrated the existence of cortical projections to M1, mainly originating from the primary somatosensory region in the same hemisphere[77,78]. Moreover, the primary somatosensory cortex is part of a complex intra-cortical and cortico-thalamo-cortical network which facilitates the flow of sensory information[79]. Another retrograde tracer injection study revealed the existence of thalamocortical projections ascending through the caudate putamen or directly from the ventral posterolateral thalamic nucleus to the primary and secondary somatosensory cortices, while the latter cortices were shown to be reciprocally connected[80]. Cortical afferents from S1 and M1 to the CPu were suggested as mediators for sensorimotor integration in the basal ganglia using tracer anterograde labeling[81], while somatosensory processing in a task of whisker pad stimulation was shown to trigger hippocampal responses in electrophysiological recordings[82]. From the perspective of BOLD, positive responses were measured in S2[69,70,72–76] and Tha contralaterally[72,75,76] or bilaterally[69,73,74], whereas a negative BOLD response was reported bilaterally in the CPu[72,74]. None of these studies reported any BOLD response in the hippocampal subfields. Globally, the entirety of this body of literature strongly indicates that brain activity during somatosensory processing extends well beyond S1FL and is relevantly captured by MD and/or MK changes in our study.

4.2 Microstructural dynamics underlying MD and MK changes in S1FL and M1

The observed MD and MK changes we report reflect the collective impact of numerous microscopic processes (e.g., geometric changes in the intra- and extracellular spaces resulting from cellular swelling, increased tortuosity and restrictions in the extracellular space, decreased restrictions in the intracellular space, decreased transmembrane permeability, etc.) occurring simultaneously across multiple spatial scales.

The measured MD drop in S1FL and M1 during the stimulus condition was previously reported in human[14,20] and rodent[21,22] studies, and was attributed to cellular swelling and increased tortuosity in the extracellular space. While the precise mechanisms underlying an MD reduction during neural activity remain unclear, functional-induced alterations in water diffusivity may exhibit varying patterns contingent upon the cellular structure(s) or the spatial scale under investigation. For example, in the *Aplysia Californica* buccal ganglia, water diffusivity was reported to increase inside neuronal soma and decrease at the level of the whole tissue upon

cellular swelling[83,84], while a closer look at water diffusivity in the synaptic microenvironment revealed a tenfold increase near the excitatory synapses, in contrast to regions farther away from the synaptic site[85]. In our study, time-dependence analyses of MD(Δ) were expected to bring more insight into the intracellular vs. extracellular contributions behind the stimulus-induced MD changes, but the power-law fit for structural disorder did not allow us to unambiguously disentangle between these possible contributions. Similar AICc and fit coefficients were obtained for the rest and stimulus conditions in the case of 1D structural disorder (**Table 3**), suggesting that the MD drop is not driven by structural disorder changes in the intracellular compartment. However, the estimation errors on the power-law parameters were overall too large to make further inferences.

As for MK, our initial hypothesis posited that it could capture the alterations in trans-membrane permeability linked to the regulation of imbalances induced by physiological and biochemical processes accompanying action potential propagation and synaptic transmission[37,86–89]. Notably, the genesis of advanced diffusion biophysical models for gray matter tissues such as NEXI[39,40,42] was prompted by the imperative to address the impact of exchange between the intra- and extracellular compartments on diffusion-weighted signals. Consequently, the imprint of exchange in gray matter is ingrained within the dMRI signal. As such, the measured MK reduction in contralateral S1FL suggested an increase in trans-membrane permeability resulting from reduced water compartmentalization, further confirmed by the slight decrease in the estimated exchange time from MK(Δ) time-dependent analyses. However, both 1D structural disorder and exchange contribute to the MK time-dependence as suggested by the comparable AICc values (**Table 4**), thus possibly overshadowing an even larger effect of the neural activation on the exchange time. Furthermore, a reduction in intra-compartment kurtosis contributing to the net MK decrease cannot be ruled out.

4.3 Microstructural dynamics underlying MD and MK changes in S2 and subcortical areas

Interestingly, findings in S1FL and M1 were contrasted by the increase in MD and MK in S2 and the subcortical ROIs, possibly reflecting an opposite signature in terms of water mobility across the microstructure, e.g. a different excitatory/inhibitory balance, for the latter brain regions. Indeed, sensorimotor signals were shown to initiate both excitation and inhibition processes in the various hippocampal subfields[82], an inhibitory postsynaptic potential was reported in various thalamic nuclei[90], while the striatum is one of the main hubs for inhibitory interneurons[81,91]. S2 may not be directly associated with an inhibitory response, but projections from both thalamic nuclei and S1 to S2 might result in both inhibitory and excitatory

responses. As for the underlying mechanisms explaining a dominant MD increase during inhibitory/excitatory balance, cellular shrinkage associated with neuronal hyperpolarization[9] is one possible hypothesis, while reduced trans-membrane water transport in the hyperpolarized state could be at the origin of an increase in MK. However, as suggested by a recent study focusing on the rat and human striatum[92], the polarity of the functional response as measured by BOLD cannot be solely explained by neuronal activity subcortically, i.e. positive BOLD = excitatory activity and negative BOLD = inhibitory activity, but rather by complex neurochemical feed-forward mechanisms. A different neurochemical environment across the various brain regions involved in somatosensory processing and integration could also have an impact on water diffusivity, and thus lead to the observed MD and MK trends. An alternative hypothesis would involve a region-dependent shift in the dominant mechanisms or water compartmentalization influencing MD and MK. Notably, astrocytes behave as excellent osmometers[93] and play an important role in brain excitability[94]. The astrocytic density is higher in subcortical regions than in the cerebral cortex in the adult rat brain[95] and changes in astrocyte volume were shown to be dependent on the degree of hypoosmolality of their surrounding medium[96], with a direct link between astrocyte volume regulation and membrane permeability[97]. Nonetheless, additional studies are warranted to elucidate the precise mechanism at play and their specific relationship with MD and MK.

4.4 Dissociation between BOLD and diffusion changes and their respective sensitivities

As previously stated, MD and MK changes during stimulation did not parallel BOLD signal modifications in a systematic way. In contralateral S1FL and M1, the average BOLD signal increase was paired by a decrease in MK and/or MD, while ipsilateral S1FL presented a decrease in MD in the absence of detectable BOLD signal variations. On the other hand, a weak negative BOLD signal was accompanied by strongly significant elevations of MD and MK in the CPu. In the remaining brain regions, the trends were dissociated: the BOLD signal and MD increased in contralateral S2, while no significant BOLD change were found in ipsilateral S2, bilateral Tha or Hip in the presence of an increase in MD and MK. The absolute amplitude of the BOLD signal changes scaled with the expected functional involvement of each area, with the highest response in S1FL (1.2%) and gradually less in S2 (0.3%), M1 (0.2%) and CPu (0.1%), although whether the order between S2, M1 and CPu reflects the actual strength of functional activity is not known. Intriguingly, the absolute amplitude of the significant MD and MK changes was overall above 1%, except for MD in the ipsilateral S1FL. The absolute maximum amplitude changes for MD were weaker in S1FL and M1 (1.1%/1.2%) than in areas of MD increase, such as S2 or Tha (1.5%/1.9%). On the other hand, contralateral S1FL showed a marked absolute MK variation (maximum of 4.9%) while the

absolute amplitude of the significant changes in Tha and Hip was reduced by half (maximum of 2.4%). While contralateral S1FL is undoubtedly the area of strongest excitatory activity in this task, it remains to be established if the comparable MD amplitude changes between S1FL and subcortical regions are the result of competing mechanisms that contribute to either an increase or decrease in MD, or a possibly strong inhibitory response in subcortical regions.

Measuring significant diffusion changes below the BOLD detection threshold indicates a higher sensitivity for MD and MK to brain activity, although it is possible that the neurovascular responses in the subcortical areas were potentially too weak to be detected with our experimental setup. Indeed, the acquired dMRI and BOLD-fMRI images reflect the sensitivity profile of a surface coil, with reduced SNR in the deeper brain regions as compared to the cortex. However, both GE-EPI and PGSE-EPI were affected by this profile, with the spin-echo diffusion images possibly even more affected due to larger flip angles and relative inefficiency of the refocusing pulse far from the coil. Furthermore, the GE-EPI sequence was optimized for BOLD sensitivity, following previously established and recommended protocols[49,98]. Beyond GLM voxel-wise analyses, we attempted to match the sensitivity of BOLD and MD/MK by averaging the BOLD signal across all rest and stimulus intervals for each anatomical ROI. In spite of this, we report an increase in MD and MK in the thalamus and the hippocampus, in the absence of a notable BOLD signal change.

Furthermore, changes in the diffusion metrics remained specific to regions involved in the somatosensory processing and integration, as no MD or MK changes were observed in cortical regions such as ACC, RSC, PPC or M2 which were also devoid of a BOLD response.

4.5 Limitations - dMRI

The fast kurtosis approach[47] used to estimate MD and MK in a scan time compatible with a functional block design is certainly associated with higher estimation uncertainty as compared to the full kurtosis tensor estimation. In practice, a 'classical' protocol for diffusion and kurtosis tensor estimation comprises approximately 30 directions per b-value, well superior to the nine directions per b-value acquired in this study. In addition, the higher intrinsic sensitivity to noise for the kurtosis metrics led to a relatively large MK uncertainty, which also translated into fewer ROIs displaying a significant change in MK as compared to MD. Thus, the analysis of time-dependent MK(Δ) was likely confounded not just by concomitant contributions between structural disorder and exchange, but also by the limited precision of fast MK estimates. Ideally, future studies would employ microstructural biophysical models, such as NEXI[39,40,42], to enable access to compartment-specific water diffusivity changes associated with neural activity.

Another limitation is the possible BOLD-like contribution to MD and MK estimates, i.e. driven by changes in blood volume and oxygenation that cause susceptibility changes in the surrounding tissues. However, working with MD and MK vs. diffusion-weighted signals largely cancels out T_2-weighting that can otherwise reflect BOLD contrast. In addition, the shorter T_2 of blood at high magnetic fields (here, 14.1T) reduces the direct intravascular water contribution to the dMRI signal. Nevertheless, the interaction between diffusion-weighting gradients and susceptibility-induced background gradient fields around blood vessels becomes much more significant at high field strength. The latter effect can lead to an increase in apparent diffusivity, and was previously shown to have a higher impact in the standard Stejskal-Tanner spin-echo diffusion weighting[99]. The use of a PGSE-EPI sequence is therefore also a limitation in the current work. Unfortunately, a twice refocused spin-echo (TRSE) sequence[100] compensated for cross-term contributions would have resulted in a prohibitively long echo time. The implications of a potential BOLD-like contribution to MD changes during stimulation are however not very far reaching for our data. Indeed, in areas with the highest BOLD positive amplitudes (S1FL, S2, M1), we reported a decrease in MD and MK, rather than an increase. Brain regions displaying an increase in MD during stimulation were accompanied either by an increase in BOLD signal (contralateral S2), a weak decrease (contralateral CPu) or no BOLD response at all (ipsilateral S2 and Cpu, bilateral Tha and Hip). The proof that task-driven MD and MK changes are not dependent on vascular response but are instead associated with changes in cellular microstructure remains valid.

4.6 Limitations – BOLD-fMRI

Factors such as magnetic field strength[101], echo time[102] and temporal SNR (tSNR)[103] all influence BOLD sensitivity. In this study, we leveraged the advantages of an ultra-high magnetic field system to enhance BOLD sensitivity, and the echo time was optimally set according to a recently published consensus protocol for functional connectivity analysis in the rat brain[98]. Nonetheless, lower T_2* in subcortical brain regions[74] resulting from differences in vascular organization[104] and susceptibility effects as compared to cortical areas, might prompt the need for a different echo time in order to maximize BOLD sensitivity subcortically. The use of a surface transceiver RF coil in our study led to a notable tSNR reduction in the deeper structures of the brain, possibly obscuring weaker BOLD changes. However, the same penalty applied for the diffusion-weighted images. New approaches for the analysis of BOLD-fMRI time-series employing response function tailored[105,106] by region, task and/or subject could be used in the future for a more robust detection of voxel-wise significant BOLD signal changes beyond the main activated brain regions.

5. CONCLUSIONS

To conclude, in this study we have shown an MD and MK reduction during brain activity in contralateral S1FL consistent with changes in cellular morphology and water transport mechanisms, paired with a positive BOLD response. As the MD and MK changes between the rest and stimulus conditions did not parallel the BOLD signal dynamics in a systematic way in all the investigated brain regions, the current study demonstrates the potential of MD and MK to provide complementary functional information to BOLD across multiple cortical and subcortical areas in the rat brain. Remarkably, MD and MK detected functional-induced changes in areas reported in the literature as part of the somatosensory processing and integration pathways, with overall higher sensitivity than BOLD. Future research endeavors will focus on delving deeper into the underlying mechanisms behind the elevation in MD and MK associated with neural activity, particularly as observed in S2 and subcortically.

6. REFERENCES

1. Sokoloff L. Local Cerebral Energy Metabolism: Its Relationships to Local Functional Activity and Blood Flow. In: *Ciba Foundation Symposium 56 - Cerebral Vascular Smooth Muscle and Its Control*. John Wiley & Sons, Ltd; 1978:171-197. doi:10.1002/9780470720370.ch10

2. Ogawa S, Lee TM, Kay AR, Tank DW. Brain magnetic resonance imaging with contrast dependent on blood oxygenation. *Proc Natl Acad Sci*. 1990;87(24):9868-9872. doi:10.1073/pnas.87.24.9868

3. Matthews PM, Jezzard P. Functional magnetic resonance imaging. *J Neurol Neurosurg Psychiatry*. 2004;75(1):6-12.

4. Morita T, Asada M, Naito E. Contribution of Neuroimaging Studies to Understanding Development of Human Cognitive Brain Functions. *Front Hum Neurosci*. 2016;10. https://www.frontiersin.org/articles/10.3389/fnhum.2016.00464. Accessed January 19, 2024.

5. Tasaki I, Byrne PM. Rapid structural chances in nerve fibers evoked by electric current pulses. *Biochem Biophys Res Commun*. 1992;188(2):559-564. doi:10.1016/0006-291X(92)91092-5

6. Saly V, Andrew RD. CA3 neuron excitation and epileptiform discharge are sensitive to osmolality. *J Neurophysiol*. 1993;69(6):2200-2208. doi:10.1152/jn.1993.69.6.2200

7. Andrew RD, Macvicar BA. Imaging cell volume changes and neuronal excitation in the hippocampal slice. *Neuroscience*. 1994;62(2):371-383. doi:10.1016/0306-4522(94)90372-7

8. Sun JY, Wu LG. Fast Kinetics of Exocytosis Revealed by Simultaneous Measurements of Presynaptic Capacitance and Postsynaptic Currents at a Central Synapse. *Neuron*. 2001;30(1):171-182. doi:10.1016/S0896-6273(01)00271-9

9. Fraser JA, Huang CLH. A quantitative analysis of cell volume and resting potential determination and regulation in excitable cells. *J Physiol*. 2004;559(2):459-478. doi:10.1113/jphysiol.2004.065706

10. Chéreau R, Saraceno GE, Angibaud J, Cattaert D, Nägerl UV. Superresolution imaging reveals activity-dependent plasticity of axon morphology linked to changes in action potential conduction velocity. *Proc Natl Acad Sci*. 2017;114(6):1401-1406. doi:10.1073/pnas.1607541114

11. Costa AR, Pinto-Costa R, Sousa SC, Sousa MM. The Regulation of Axon Diameter: From Axonal Circumferential Contractility to Activity-Dependent Axon Swelling. *Front Mol Neurosci*. 2018;11. https://www.frontiersin.org/articles/10.3389/fnmol.2018.00319. Accessed November 21, 2023.

12. Ling T, Boyle KC, Zuckerman V, et al. High-speed interferometric imaging reveals dynamics of neuronal deformation during the action potential. *Proc Natl Acad Sci*. 2020;117(19):10278-10285. doi:10.1073/pnas.1920039117

13. Kwon J, Lee S, Jo Y, Choi M. All-optical observation on activity-dependent nanoscale dynamics of myelinated axons. *Neurophotonics*. 2023;10(01). doi:10.1117/1.NPh.10.1.015003

14. Le Bihan D, Urayama S ichi, Aso T, Hanakawa T, Fukuyama H. Direct and fast detection of neuronal activation in the human brain with diffusion MRI. *Proc Natl Acad Sci*. 2006;103(21):8263-8268. doi:10.1073/pnas.0600644103

15. Aso T, Urayama SI, Fukuyama H, Le Bihan D. Comparison of diffusion-weighted fMRI and BOLD fMRI responses in a verbal working memory task. *NeuroImage*. 2013;67:25-32. doi:10.1016/j.neuroimage.2012.11.005

16. Norris DG. Spin-echo fMRI: The poor relation? *NeuroImage*. 2012;62(2):1109-1115. doi:10.1016/j.neuroimage.2012.01.003

17. Buxton RB, Wong EC, Frank LR. Dynamics of blood flow and oxygenation changes during brain activation: The balloon model. *Magn Reson Med*. 1998;39(6):855-864. doi:10.1002/mrm.1910390602

18. Friston KJ, Mechelli A, Turner R, Price CJ. Nonlinear Responses in fMRI: The Balloon Model, Volterra Kernels, and Other Hemodynamics. *NeuroImage*. 2000;12(4):466-477. doi:10.1006/nimg.2000.0630

19. Sundqvist N, Sten S, Thompson P, Andersson BJ, Engström M, Cedersund G. Mechanistic model for human brain metabolism and its connection to the neurovascular coupling. *PLOS Comput Biol*. 2022;18(12):e1010798. doi:10.1371/journal.pcbi.1010798

20. Darquié A, Poline JB, Poupon C, Saint-Jalmes H, Le Bihan D. Transient decrease in water diffusion observed in human occipital cortex during visual stimulation. *Proc Natl Acad Sci*. 2001;98(16):9391-9395. doi:10.1073/pnas.151125698

21. Tsurugizawa T, Ciobanu L, Le Bihan D. Water diffusion in brain cortex closely tracks underlying neuronal activity. *Proc Natl Acad Sci*. 2013;110(28):11636-11641. doi:10.1073/pnas.1303178110

22. Abe Y, Tsurugizawa T, Bihan DL. Water diffusion closely reveals neural activity status in rat brain loci affected by anesthesia. *PLOS Biol*. 2017;15(4):e2001494. doi:10.1371/journal.pbio.2001494

23. Miller KL, Bulte DP, Devlin H, et al. Evidence for a vascular contribution to diffusion FMRI at high b value. *Proc Natl Acad Sci*. 2007;104(52):20967-20972. doi:10.1073/pnas.0707257105

24. Kuroiwa D, Obata T, Kawaguchi H, et al. Signal contributions to heavily diffusion-weighted functional magnetic resonance imaging investigated with multi-SE-EPI acquisitions. *NeuroImage*. 2014;98:258-265. doi:10.1016/j.neuroimage.2014.04.050

25. Williams RJ, Reutens DC, Hocking J. Influence of BOLD Contributions to Diffusion fMRI Activation of the Visual Cortex. *Front Neurosci*. 2016;10. https://www.frontiersin.org/articles/10.3389/fnins.2016.00279. Accessed January 27, 2024.

26. Bai R, Stewart CV, Plenz D, Basser PJ. Assessing the sensitivity of diffusion MRI to detect neuronal activity directly. *Proc Natl Acad Sci*. 2016;113(12):E1728-E1737. doi:10.1073/pnas.1519890113

27. Nunes D, Ianus A, Shemesh N. Layer-specific connectivity revealed by diffusion-weighted functional MRI in the rat thalamocortical pathway. *NeuroImage*. 2019;184:646-657. doi:10.1016/j.neuroimage.2018.09.050

28. Nunes D, Gil R, Shemesh N. A rapid-onset diffusion functional MRI signal reflects neuromorphological coupling dynamics. *NeuroImage*. 2021;231:117862. doi:10.1016/j.neuroimage.2021.117862

29. Olszowy W, Diao Y, Jelescu IO. Beyond BOLD: Evidence for diffusion fMRI contrast in the human brain distinct from neurovascular response. June 2021:2021.05.16.444253. doi:10.1101/2021.05.16.444253

30. Yacoub E, Uludağ K, Uğurbil K, Harel N. Decreases in ADC observed in tissue areas during activation in cat visual cortex at 9.4 T using high diffusion sensitization. *Magn Reson Imaging*. 2008;26(7):889-896. doi:10.1016/j.mri.2008.01.046

31. Flint J, Hansen B, Vestergaard-Poulsen P, Blackband SJ. Diffusion weighted magnetic resonance imaging of neuronal activity in the hippocampal slice model. *NeuroImage*. 2009;46(2):411-418. doi:10.1016/j.neuroimage.2009.02.003

32. Tirosh N, Nevo U. Neuronal activity significantly reduces water displacement: DWI of a vital rat spinal cord with no hemodynamic effect. *NeuroImage*. 2013;76:98-107. doi:10.1016/j.neuroimage.2013.02.065

33. Spees WM, Lin TH, Song SK. White-matter diffusion fMRI of mouse optic nerve. *NeuroImage*. 2013;65:209-215. doi:10.1016/j.neuroimage.2012.10.021

34. Lin TH, Spees WM, Chiang CW, Trinkaus K, Cross AH, Song SK. Diffusion fMRI detects white-matter dysfunction in mice with acute optic neuritis. *Neurobiol Dis*. 2014;67:1-8. doi:10.1016/j.nbd.2014.02.007

35. Badaut J, Ashwal S, Adami A, et al. Brain Water Mobility Decreases after Astrocytic Aquaporin-4 Inhibition Using RNA Interference. *J Cereb Blood Flow Metab*. 2011;31(3):819-831. doi:10.1038/jcbfm.2010.163

36. Pavlin T, Nagelhus EA, Brekken C, et al. Loss or Mislocalization of Aquaporin-4 Affects Diffusion Properties and Intermediary Metabolism in Gray Matter of Mice. *Neurochem Res*. 2017;42(1):77-91. doi:10.1007/s11064-016-2139-y

37. Bai R, Springer CS, Plenz D, Basser PJ. Brain active transmembrane water cycling measured by MR is associated with neuronal activity. *Magn Reson Med*. 2019;81(2):1280-1295. doi:10.1002/mrm.27473

38. Lee HH, Papaioannou A, Novikov DS, Fieremans E. In vivo observation and biophysical interpretation of time-dependent diffusion in human cortical gray matter. *NeuroImage*. 2020;222:117054. doi:10.1016/j.neuroimage.2020.117054

39. Jelescu IO, de Skowronski A, Geffroy F, Palombo M, Novikov DS. Neurite Exchange Imaging (NEXI): A minimal model of diffusion in gray matter with inter-compartment water exchange. *NeuroImage*. 2022;256:119277. doi:10.1016/j.neuroimage.2022.119277

40. Olesen JL, Østergaard L, Shemesh N, Jespersen SN. Diffusion time dependence, power-law scaling, and exchange in gray matter. *Neuroimage*. 2022;251:118976. doi:10.1016/j.neuroimage.2022.118976

41. Mougel E, Valette J, Palombo M. Investigating exchange, structural disorder and restriction in Gray Matter via water and metabolites diffusivity and kurtosis time-dependence. In: London, England, UK; :0255. doi:10.58530/2022/0255

42. Uhl Q, Pavan T, Molendowska M, Jones DK, Palombo M, Jelescu I. Quantifying human gray matter microstructure using Neurite Exchange Imaging (NEXI) and 300 mT/m gradients. *Imaging Neurosci*. February 2024. doi:10.1162/imag_a_00104

43. Novikov DS, Jensen JH, Helpern JA, Fieremans E. Revealing mesoscopic structural universality with diffusion. *Proc Natl Acad Sci*. 2014;111(14):5088-5093. doi:10.1073/pnas.1316944111

44. Kärger J. NMR self-diffusion studies in heterogeneous systems. *Adv Colloid Interface Sci*. 1985;23:129-148. doi:10.1016/0001-8686(85)80018-X

45. Jensen JH, Helpern JA, Ramani A, Lu H, Kaczynski K. Diffusional kurtosis imaging: The quantification of non-gaussian water diffusion by means of magnetic resonance imaging. *Magn Reson Med*. 2005;53(6):1432-1440. doi:10.1002/mrm.20508

46. Wu EX, Cheung MM. MR diffusion kurtosis imaging for neural tissue characterization. *NMR Biomed*. 2010;23(7):836-848. doi:10.1002/nbm.1506

47. Hansen B, Lund TE, Sangill R, Stubbe E, Finsterbusch J, Jespersen SN. Experimental considerations for fast kurtosis imaging. *Magn Reson Med*. 2016;76(5):1455-1468. doi:10.1002/mrm.26055

48. Hansen B, Shemesh N, Jespersen SN. Fast imaging of mean, axial and radial diffusion kurtosis. *NeuroImage*. 2016;142:381-393. doi:10.1016/j.neuroimage.2016.08.022

49. Reynaud O, da Silva AR, Gruetter R, Jelescu IO. Multi-slice passband bSSFP for human and rodent fMRI at ultra-high field. *J Magn Reson*. 2019;305:31-40. doi:10.1016/j.jmr.2019.05.010

50. Veraart J, Fieremans E, Novikov DS. Diffusion MRI noise mapping using random matrix theory. *Magn Reson Med*. 2016;76(5):1582-1593. doi:10.1002/mrm.26059

51. Tournier JD, Smith R, Raffelt D, et al. MRtrix3: A fast, flexible and open software framework for medical image processing and visualisation. *NeuroImage*. 2019;202:116137. doi:10.1016/j.neuroimage.2019.116137

52. Kellner E, Dhital B, Kiselev VG, Reisert M. Gibbs-ringing artifact removal based on local subvoxel-shifts. *Magn Reson Med*. 2016;76(5):1574-1581. doi:10.1002/mrm.26054

53. Andersson JLR, Skare S, Ashburner J. How to correct susceptibility distortions in spin-echo echo-planar images: application to diffusion tensor imaging. *NeuroImage*. 2003;20(2):870-888. doi:10.1016/S1053-8119(03)00336-7

54. Andersson JLR, Sotiropoulos SN. An integrated approach to correction for off-resonance effects and subject movement in diffusion MR imaging. *NeuroImage*. 2016;125:1063-1078. doi:10.1016/j.neuroimage.2015.10.019

55. Lohmeier J, Kaneko T, Hamm B, Makowski MR, Okano H. atlasBREX: Automated template-derived brain extraction in animal MRI. *Sci Rep*. 2019;9(1):12219. doi:10.1038/s41598-019-48489-3

56. Avants BB, Tustison N, Song G. Advanced Normalization Tools (ANTS). *Insight J*. 2009;2:1-35.

57. Tustison NJ, Avants BB, Cook PA, et al. N4ITK: Improved N3 Bias Correction. *IEEE Trans Med Imaging*. 2010;29(6):1310-1320. doi:10.1109/TMI.2010.2046908

58. Papp EA, Leergaard TB, Calabrese E, Johnson GA, Bjaalie JG. Waxholm Space atlas of the Sprague Dawley rat brain. *NeuroImage*. 2014;97:374-386. doi:10.1016/j.neuroimage.2014.04.001

59. Bates D, Mächler M, Bolker B, Walker S. Fitting Linear Mixed-Effects Models Using lme4. *J Stat Softw*. 2015;67:1-48. doi:10.18637/jss.v067.i01

60. Bock C, Krep H, Brinker G, Hoehn-Berlage M. Brainmapping of α-chloralose anesthetized rats with T2*-weighted imaging: distinction between the representation of the forepaw and hindpaw in the somatosensory cortex. *NMR Biomed*. 1998;11(3):115-119. doi:10.1002/(SICI)1099-1492(199805)11:3<115::AID-NBM526>3.0.CO;2-K

61. Brinker G, Bock C, Busch E, Krep H, Hossmann KA, Hoehn-Berlage M. Simultaneous recording of evoked potentials and T-weighted MR images during somatosensory stimulation of rat. *Magn Reson Med*. 1999;41(3):469-473. doi:10.1002/(SICI)1522-2594(199903)41:3<469::AID-MRM7>3.0.CO;2-9

62. Spenger C, Josephson A, Klason T, et al. Functional MRI at 4.7 tesla of the rat brain during electric stimulation of forepaw, hindpaw, or tail in single- and multislice experiments. *Exp Neurol*. 2000;166(2):246-253. doi:10.1006/exnr.2000.7524

63. Masamoto K, Kim T, Fukuda M, Wang P, Kim SG. Relationship between Neural, Vascular, and BOLD Signals in Isoflurane-Anesthetized Rat Somatosensory Cortex. *Cereb Cortex*. 2006;17(4):942-950. doi:10.1093/cercor/bhl005

64. Pelled G, Bergstrom DA, Tierney PL, et al. Ipsilateral cortical fMRI responses after peripheral nerve damage in rats reflect increased interneuron activity. *Proc Natl Acad Sci*. 2009;106(33):14114-14119. doi:10.1073/pnas.0903153106

65. Kim T, Masamoto K, Fukuda M, Vazquez A, Kim SG. Frequency-dependent Neural Activity, CBF, and BOLD fMRI to Somatosensory Stimuli in Isoflurane-anesthetized Rats. *NeuroImage*. 2010;52(1):224-233. doi:10.1016/j.neuroimage.2010.03.064

66. Adamczak JM, Farr TD, Seehafer JU, Kalthoff D, Hoehn M. High field BOLD response to forepaw stimulation in the mouse. *NeuroImage*. 2010;51(2):704-712. doi:10.1016/j.neuroimage.2010.02.083

67. Goloshevsky AG, Wu CWH, Dodd SJ, Koretsky AP. Mapping cortical representations of the rodent forepaw and hindpaw with BOLD fMRI reveals two spatial boundaries. *NeuroImage*. 2011;57(2):526-538. doi:10.1016/j.neuroimage.2011.04.002

68. Baltes C, Bosshard S, Mueggler T, Ratering D, Rudin M. Increased blood oxygen level-dependent (BOLD) sensitivity in the mouse somatosensory cortex during electrical forepaw stimulation using a cryogenic radiofrequency probe. *NMR Biomed*. 2011;24(4):439-446. doi:10.1002/nbm.1613

69. Keilholz SD, Silva AC, Raman M, Merkle H, Koretsky AP. Functional MRI of the rodent somatosensory pathway using multislice echo planar imaging. *Magn Reson Med*. 2004;52(1):89-99. doi:10.1002/mrm.20114

70. Weber R, Ramos-Cabrer P, Wiedermann D, van Camp N, Hoehn M. A fully noninvasive and robust experimental protocol for longitudinal fMRI studies in the rat. *NeuroImage*. 2006;29(4):1303-1310. doi:10.1016/j.neuroimage.2005.08.028

71. Cho YR, Pawela CP, Li R, et al. Refining the Sensory and Motor Ratunculus of the Rat Upper Extremity Using fMRI and Direct Nerve Stimulation. *Magn Reson Med Off J Soc Magn Reson Med Soc Magn Reson Med*. 2007;58(5):901-909. doi:10.1002/mrm.21408

72. Zhao F, Zhao T, Zhou L, Wu Q, Hu X. BOLD study of stimulation-induced neural activity and resting-state connectivity in medetomidine-sedated rat. *NeuroImage*. 2008;39(1):248-260. doi:10.1016/j.neuroimage.2007.07.063

73. Bosshard SC, Baltes C, Wyss MT, Mueggler T, Weber B, Rudin M. Assessment of brain responses to innocuous and noxious electrical forepaw stimulation in mice using BOLD fMRI. *Pain*. 2010;151(3):655-663. doi:10.1016/j.pain.2010.08.025

74. Boussida S, Traoré AS, Durif F. Mapping of the brain hemodynamic responses to sensorimotor stimulation in a rodent model: A BOLD fMRI study. *PLOS ONE*. 2017;12(4):e0176512. doi:10.1371/journal.pone.0176512

75. Jung WB, Shim HJ, Kim SG. Mouse BOLD fMRI at ultrahigh field detects somatosensory networks including thalamic nuclei. *NeuroImage*. 2019;195:203-214. doi:10.1016/j.neuroimage.2019.03.063

76. Jung WB, Im GH, Jiang H, Kim SG. Early fMRI responses to somatosensory and optogenetic stimulation reflect neural information flow. *Proc Natl Acad Sci*. 2021;118(11):e2023265118. doi:10.1073/pnas.2023265118

77. Colechio EM, Alloway KD. Differential topography of the bilateral cortical projections to the whisker and forepaw regions in rat motor cortex. *Brain Struct Funct*. 2009;213(4):423-439. doi:10.1007/s00429-009-0215-7

78. Yamawaki N, Raineri Tapies MG, Stults A, Smith GA, Shepherd GM. Circuit organization of the excitatory sensorimotor loop through hand/forelimb S1 and M1. Brown SP, Calabrese RL, Connors B, Yoshida Y, eds. *eLife*. 2021;10:e66836. doi:10.7554/eLife.66836

79. Jabaudon D. Fate and freedom in developing neocortical circuits. *Nat Commun*. 2017;8:16042. doi:10.1038/ncomms16042

80. Liao CC, Yen CT. Functional Connectivity of the Secondary Somatosensory Cortex of the Rat. *Anat Rec Adv Integr Anat Evol Biol*. 2008;291(8):960-973. doi:10.1002/ar.20696

81. Ramanathan S, Hanley JJ, Deniau JM, Bolam JP. Synaptic Convergence of Motor and Somatosensory Cortical Afferents onto GABAergic Interneurons in the Rat Striatum. *J Neurosci*. 2002;22(18):8158-8169. doi:10.1523/JNEUROSCI.22-18-08158.2002

82. Bellistri E, Aguilar J, Brotons-Mas JR, Foffani G, de la Prida LM. Basic properties of somatosensory-evoked responses in the dorsal hippocampus of the rat. *J Physiol*. 2013;591(Pt 10):2667-2686. doi:10.1113/jphysiol.2013.251892

83. Jelescu IO, Ciobanu L, Geffroy F, Marquet P, Le Bihan D. Effects of hypotonic stress and ouabain on the apparent diffusion coefficient of water at cellular and tissue levels in Aplysia. *NMR Biomed*. 2014;27(3):280-290. doi:10.1002/nbm.3061

84. Abe Y, Van Nguyen K, Tsurugizawa T, Ciobanu L, Le Bihan D. Modulation of water diffusion by activation-induced neural cell swelling in Aplysia Californica. *Sci Rep*. 2017;7(1):6178. doi:10.1038/s41598-017-05586-5

85. Paviolo C, Ferreira JS, Lee A, et al. Near-Infrared Carbon Nanotube Tracking Reveals the Nanoscale Extracellular Space around Synapses. *Nano Lett*. 2022;22(17):6849-6856. doi:10.1021/acs.nanolett.1c04259

86. Kitaura H, Tsujita M, Huber VJ, et al. Activity-dependent glial swelling is impaired in aquaporin-4 knockout mice. *Neurosci Res*. 2009;64(2):208-212. doi:10.1016/j.neures.2009.03.002

87. Bai R, Springer Jr. CS, Plenz D, Basser PJ. Fast, Na+/K+ pump driven, steady-state transcytolemmal water exchange in neuronal tissue: A study of rat brain cortical cultures. *Magn Reson Med*. 2018;79(6):3207-3217. doi:10.1002/mrm.26980

88. Bellot-Saez A, Kékesi O, Morley JW, Buskila Y. Astrocytic modulation of neuronal excitability through K+ spatial buffering. *Neurosci Biobehav Rev*. 2017;77:87-97. doi:10.1016/j.neubiorev.2017.03.002

89. Didier MEP, Tarun OB, Jourdain P, Magistretti P, Roke S. Membrane water for probing neuronal membrane potentials and ionic fluxes at the single cell level. *Nat Commun*. 2018;9(1):5287. doi:10.1038/s41467-018-07713-w

90. O'Reilly C, Iavarone E, Yi J, Hill SL. Rodent somatosensory thalamocortical circuitry: Neurons, synapses, and connectivity. *Neurosci Biobehav Rev*. 2021;126:213-235. doi:10.1016/j.neubiorev.2021.03.015

91. Fahn S, Jankovic J, Hallett M. Chapter 3 - Functional neuroanatomy of the basal ganglia. In: Fahn S, Jankovic J, Hallett M, eds. *Principles and Practice of Movement Disorders (Second Edition)*. Edinburgh: W.B. Saunders; 2011:55-65. doi:10.1016/B978-1-4377-2369-4.00003-2

92. Cerri DH, Albaugh DL, Walton LR, et al. Distinct neurochemical influences on fMRI response polarity in the striatum. *Nat Commun*. 2024;15(1):1916. doi:10.1038/s41467-024-46088-z

93. Hellas JA, Andrew RD. Neuronal Swelling: A Non-osmotic Consequence of Spreading Depolarization. *Neurocrit Care*. 2021;35(Suppl 2):112-134. doi:10.1007/s12028-021-01326-w

94. Schwartzkroin PA, Baraban SC, Hochman DW. Osmolarity, ionic flux, and changes in brain excitability. *Epilepsy Res*. 1998;32(1):275-285. doi:10.1016/S0920-1211(98)00058-8

95. Savchenko VL, McKanna JA, Nikonenko IR, Skibo GG. Microglia and astrocytes in the adult rat brain: comparative immunocytochemical analysis demonstrates the efficacy of lipocortin 1 immunoreactivity. *Neuroscience*. 2000;96(1):195-203. doi:10.1016/s0306-4522(99)00538-2

96. Lafrenaye AD, Simard JM. Bursting at the Seams: Molecular Mechanisms Mediating Astrocyte Swelling. *Int J Mol Sci*. 2019;20(2):330. doi:10.3390/ijms20020330

97. Solenov E, Watanabe H, Manley GT, Verkman AS. Sevenfold-reduced osmotic water permeability in primary astrocyte cultures from AQP-4-deficient mice, measured by a fluorescence quenching method. *Am J Physiol-Cell Physiol*. 2004;286(2):C426-C432. doi:10.1152/ajpcell.00298.2003

98. Grandjean J, Desrosiers-Gregoire G, Anckaerts C, et al. A consensus protocol for functional connectivity analysis in the rat brain. *Nat Neurosci*. 2023;26(4):673-681. doi:10.1038/s41593-023-01286-8

99. Pampel A, Jochimsen TH, Möller HE. BOLD background gradient contributions in diffusion-weighted fMRI—comparison of spin-echo and twice-refocused spin-echo sequences. *NMR Biomed*. 2010;23(6):610-618. doi:10.1002/nbm.1502

100. Reese TG, Heid O, Weisskoff RM, Wedeen VJ. Reduction of eddy-current-induced distortion in diffusion MRI using a twice-refocused spin echo. *Magn Reson Med*. 2003;49(1):177-182. doi:10.1002/mrm.10308

101. Gati JS, Menon RS, Uğurbil K, Rutt BK. Experimental determination of the BOLD field strength dependence in vessels and tissue. *Magn Reson Med*. 1997;38(2):296-302. doi:10.1002/mrm.1910380220

102. Grüne M, Pillekamp F, Schwindt W, Hoehn M. Gradient echo time dependence and quantitative parameter maps for somatosensory activation in rats at 7 T. *Magn Reson Med*. 1999;42(1):118-126. doi:10.1002/(SICI)1522-2594(199907)42:1<118::AID-MRM16>3.0.CO;2-T

103. Murphy K, Bodurka J, Bandettini PA. How long to scan? The relationship between fMRI temporal signal to noise and necessary scan duration. *NeuroImage*. 2007;34(2):565-574. doi:10.1016/j.neuroimage.2006.09.032

104. Sloan HL, Austin VC, Blamire AM, et al. Regional differences in neurovascular coupling in rat brain as determined by fMRI and electrophysiology. *NeuroImage*. 2010;53(2):399-411. doi:10.1016/j.neuroimage.2010.07.014

105. Gonzalez-Castillo J, Saad ZS, Handwerker DA, Inati SJ, Brenowitz N, Bandettini PA. Whole-brain, time-locked activation with simple tasks revealed using massive averaging and model-free analysis. *Proc Natl Acad Sci*. 2012;109(14):5487-5492. doi:10.1073/pnas.1121049109

106. Schilling KG, Janve V, Gao Y, Stepniewska I, Landman BA, Anderson AW. Histological validation of diffusion MRI fiber orientation distributions and dispersion. *NeuroImage*. 2018;165:200-221. doi:10.1016/j.neuroimage.2017.10.046